Atomic layer deposition in porous electrodes: A pore-scale modeling study

Wen-Zhen Fang[a,b,c], Yu-Qing Tang[a], Chunmei Ban[b], Qinjun Kang[d,*], Rui Qiao[b,*], Wen-Quan Tao[a]

[a] *Key Laboratory of Thermo-Fluid Science and Engineering, MOE, Xi'an Jiaotong University, Xi'an, China*
[b] *Department of Mechanical Engineering, Virginia Tech, Blacksburg, VA 24061, USA*
[c] *School of Mechanical and Aerospace Engineering, Nanyang Technological University, Singapore*
[d] *Earth and Environmental Sciences Division, MS T003, Los Alamos National Laboratory, Los Alamos, NM 87545, USA*

HIGHLIGHTS

- 3D pore-scale reactive transport during atomic layer deposition is studied.
- Realistic porous electrodes are built and effects of microstructures are revealed.
- Accuracy of previous mean-field models is examined by pore-scale results.
- Electrodes with smaller secondary pores require a longer exposure time.
- Poorly-connected pores inside electrodes slow down the coating rate.

ARTICLE INFO

ABSTRACT

Coating porous electrodes of Li-ion batteries with functional materials by atomic layer deposition (ALD) can enhance their capacity stability. Because of the complex microstructure of the porous electrodes, predicting the required exposure time of the precursors for achieving a desired coating and the coating characteristics for a given exposure time remains difficult. Here, a three-dimensional (3D) pore-scale lattice Boltzmann model is developed to investigate the reactive transport processes during the ALD of reconstructed electrodes and to assess the accuracy of one-dimensional (1D) mean-field models. The effects of the hierarchical structure of pores and their connectivity on the coating process of ALD are investigated and the detailed coating characteristics in the electrodes are resolved. Electrodes with smaller pore sizes requires a longer exposure time to achieve full coating. At the same depth within an electrode, the smaller pores are coated more slowly than the wider pores (especially at high Damkohler numbers) and the coating speed of well-connected pores are faster than that of poorly connected pores. Simulations also reveal that the 1D mean-field model can capture the average coating characteristics reasonably well when pores in the electrodes are well connected but may perform poorly if the pores are poorly connected.

1. Introduction

Atomic layer deposition (ALD) is a thin film deposition technique based on two sequential, self-limiting surface reactions between precursors and reactive surfaces. The self-limiting nature of ALD reactions enables highly conformal deposition and exquisite control of the film thickness, thus making ALD highly effective in coating high-aspect-ratio materials. ALD has found applications in areas such as the fabrication of semiconductors and microelectromechanical systems [1–3]. Recently, ALD has been used in the preparation of Si-based electrodes for Li-ion batteries. Compared to the traditional graphite electrodes, silicon (Si) electrodes offer much higher theoretical energy capacity. However, Si

particles undergo large volume expansion during charging, which induces cracks in them and ultimately leads to rapid capacity degradation of the battery. By coating a thin film of Al_2O_3 on the surface of the Si particles in the porous electrodes, stable artificial solid electrolyte interfaces have been engineered and the resulting electrodes showed greatly enhanced capacity stability over the untreated electrodes [4,5]. These results have stirred up interest in employing ALD in Li-ion battery manufacturing.

Spatial ALD offers a higher coating rate than the temporal ALD and can be incorporated into roll-to-roll manufacturing process more easily [6]. Thus, spatial ALD is preferred for coating porous electrodes. In spatial ALD, different precursors are injected at different locations and

---

Nomenclature		s_0	Area of a surface site (m^2)
		$\bar{s}$	Specific surface area (m^{-1})
Variables		V	Volume (m^3)
C	Concentration (mol/m^3)	*Greek*	
d	Pore diameter (nm)		
D	Diffusivity (m^2/s)	α	Damkohler number
D_e	Effective diffusivity (m^2/s)	β_0	Sticking coefficient
g	Distribution function	θ	Surface coverage
L	Length (m)	γ	Number of molecules per surface site
M	Molar mass (g/mol)	ε	Porosity
n_0	Number density of precursor	ε_{con}	Effective porosity
P	Pressure (Pa)	ν_{th}	Thermal velocity
R	Universal gas constant (J/mol/K)	ω	Weight parameter
T	Temperature (K)	τ	Relaxation coefficient
t	Exposure time (s)		

the electrodes are moved to these locations (e.g., by mounting the electrode on a rotating cylinder) sequentially [7]. To ensure high quality coating in spatial ALD, the exposure time (also termed dosing time) of the porous electrodes to precursor gas must be carefully controlled so that solid surfaces are fully saturated by reactive precursor molecules. The importance of ALD time-scale analysis for porous substrates has been articulated by Granneman et al. [8], but how to predict the exposure time accurately for the complex porous substrate remains a challenge.

During the past two decades, much effort has been devoted to predict the exposure time required for ALD to coat high aspect ratio features [9–13]. Most of these models treat the ALD as a coupled reaction and transport process. Cale and Raupp [14] derived a Clausing-like integral equation governing the transport and deposition process of the low-pressure chemical vapor deposition in a closed cylindrical structure . Adomaitis [15] developed a ballistic transport model to simulate the ALD process in nanopores with large aspect ratio and discussed the coupled transport and surface reaction in detail. Gordon and co-workers [16] proposed an analytical model that can approximately predict the exposure time required to coat circular holes as a function of aspect ratio by assuming a step-function coverage profile. Their model indicates that the saturation exposure time exhibits a quadratic dependence on the aspect ratio of circular holes. However, their model neglects the effects of surface reaction kinetics and is valid only in the diffusion-limited transport regime. Later work based on Monte Carlo simulations showed that the reaction probability significantly affects the surface coverage profile of precursors and the required exposure time of ALD to achieve the surface saturation [17,18]. These simulations confirmed that, in the diffusion-limited regime, the model by Gordon and co-worker captures the required exposure time well; in the reaction-limited regime, the required exposure time is insensitive to or even independent of the aspect ratio of the feature to be coated. Most recently, by solving a one-dimensional (1D) reaction-diffusion equation, Yanguas-Gil and Elam [19] reported an analytical expression that can be used to predict the saturation exposure time in both diffusion-limited and reaction-limited regimes.

Most of the available models of ALD focus on idealized geometries such as straight pores or trenches. The ALD in porous materials, however, is more complex. Keuter et al. [20] developed a mean-field model by extending the reaction-diffusion model by Yanguas-Gil and Elam to predict the saturation exposure time for ALD in porous substrates of solid oxide fuel cells. The key idea is to model the effect of the porous microstructure on the transport of precursors by introducing an effective diffusivity of the precursor molecules in the porous substrate, which was calculated using empirical formula based on effective medium theories. The accuracy of this mean-field model remains to be clarified. Indeed, key microstructure information of real electrodes,

e.g., connectivity and pore size distribution, cannot be accurately taken into account in conventional effective medium theories, which can potentially compromise the accuracy of the mean-field ALD model based on these theories. In fact, the work by Bae et al. [21] showed that the connectivity of pores greatly affects the precursor diffusion inside porous materials and must be taken into account for accurate prediction of exposure time in ALD. Furthermore, the pore size distribution of electrodes also significantly affects the reactive transport process in ALD [22], but how these characteristics of the electrodes affect the exposure time remains unclear. To obtain an understanding of how the electrode microstructure affects the saturation exposure time and the evolution of the surface coverage profile during ALD, pore-scale simulations, in which the reactive transport processes in electrodes with realistic microstructure are resolved, are needed.

In this work, a three-dimensional (3D) pore-scale model is developed to investigate the diffusion-reaction process of ALD in porous electrodes. The diffusion-reaction equations in porous electrodes are solved numerically using the lattice Boltzmann method (LBM). Although other models, such as the finite volume method [23] and finite element method [24], can also solve the diffusion-reaction process, LBM is chosen here because its kinetic nature makes it highly effective in dealing with complex geometries [25–27] and highly efficient in parallel implementation [28,29]. The high efficiency in parallel computing is important since 3D pore-scale ALD model is computationally expensive. In this work, the message passing interface (MPI) is adopted for the parallel computing and in-house code is performed on 100 cores with Intel Xeon E5 processors.

In recent decades, LBM has been developed into an alternative and promising numerical tool to simulate the reactive transport processes involving precipitation and dissolution. Particularly, Kang et al. [30] first proposed the reactive transport model using LBM to investigate the dissolution-induced changes in porous media, and later Kang et al. [31] extended their model to multicomponent systems. Parmigiani et al. [32] developed a multiphase reactive LB model to simulate the fingering dynamics (injection of a non-wetting fluid into a wetting fluid) involving the evolution of solid geometry. Chen et al. [33] investigated reactive transport processes in two-dimensional hierarchical porous structures for catalysis applications. Gray et al. [34] coupled the LBM and finite volume method to simulate the dissolution of porous media involved in the carbon-storage injection processes.

From the above brief review, it is clear that reactive transport processes in the porous media can be solved efficiently with LBM. However, no pore-scale studies are available for the ALD process in porous substrates. In this work, the pore-scale diffusion-reaction modeling is developed for the ALD coating in porous electrodes. Our work makes unique contributions to study of ALD in three aspects: (1) it is the first pore-scale model that takes into account three-dimensional

resolved electrode microstructure during ALD, (2) the effects of microstructure (pore size distribution, secondary pores and pore connectivity) on the coating process of ALD in porous electrodes are explored, and (3) the effectiveness of the 1D mean-field model in predicting the ALD coating in porous electrodes is systematically examined with the help of the 3D pore-scale model. The fundamental insights gained through this work help guide the application of ALD in coating porous media.

2. Mathematical models and numerical methods

In the spatial ALD of a solid substrate, the substrate is typically moved continuously through chambers in which it is exposed to two alternate pulses of precursors (see Fig. 1a). This way, the two half cycles of a single ALD step are accomplished sequentially. A complete model of spatial ALD thus requires modeling the flow of carrier gas and precursor gas in the ALD chamber, the transport of the precursor molecules in the substrate (if porous), and the reactions of precursor molecules with the solid surfaces [9,35]. For porous substrates (e.g., in the ALD of porous electrodes), the saturation exposure time is limited by the reactive transport of the precursor molecules in the substrate. Therefore, in this work, we consider only the reactive transport of precursor molecules in the porous electrode during one half cycle of an ALD cycle. Because the transport of the precursor molecules in porous electrodes during ALD is typically limited by the confinement by the pore walls, the effect of carries gas flow is neglected and a constant precursor density is prescribed at the entry plane of the porous electrode.

We also make the following assumptions. (1) Because the mean free path of the precursor gas molecules is far larger than the pore size in typical ALD of porous electrodes, the gas transport is dominated by the Knudsen diffusion [15,22]; (2) An irreversible first order Langmuir surface kinetics is adopted to capture the main features during ALD, and the reaction probability β is assumed to depend linearly on the fraction of the available sites on the surface, namely $\beta = \beta_0 (1 - \theta)$, where θ is the surface coverage [19,22]; (3) Sine the time scale for evolution of the surface coverage is much longer than that of molecular diffusion, the diffusion is assumed quasi-static at each θ [19]; (4) Surface diffusion is neglected since the pore diameter is much larger than the molecular size [36].

2.1. Governing equations

2.1.1. Three-dimensional pore-scale model

In this model, the microstructure of the porous electrodes is explicitly resolved (see Fig. 1b). The transport of the precursor gas in the porous electrode is governed by the diffusion equation [22]
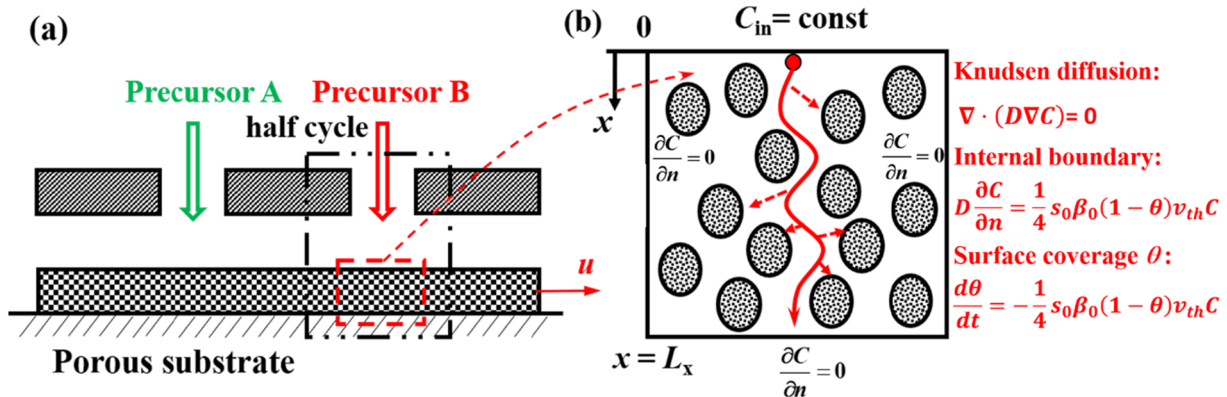
$$\frac{\partial C}{\partial t} = \nabla \cdot (D \nabla C) \tag{1}$$

where C is the concentration of the precursor gas and D is the local diffusion coefficient. D is calculated according to the local pore diameter d

$$D = \frac{d}{3} \sqrt{\frac{8RT}{\pi M}} \tag{2}$$

where R is the gas constant, T is the absolute temperature, and M is the mass of precursor molecules. Eq. (2) is effective in Knudsen diffusion regime when Knudsen number $Kn \gg 1$. Here the local Knudsen number is defined as $Kn = \lambda/d$, where λ is the mean free path of precursor molecules and d is the local pore diameter.

When precursor molecules collide with a solid surface, they can react with the active surface sites. Such reactions are described using the irreversible first order Langmuir surface kinetics. We consider that the surface has a finite number of surface sites available for reacting with precursor molecules and each site has an area s_0. The surface coverage, θ, is defined as the fraction of the available sites that have reacted with the precursor molecules. The evolution of the surface coverage is obtained by the kinetic gas theory [19,20]:

$$\frac{d\theta}{dt} = -\frac{1}{4} s_0 \beta_0 (1 - \theta) v_{th} C \tag{3}$$

where s_0 is the area of a surface site; β_0 is initial reaction probability often termed as the "sticking coefficient"; v_{th} is the mean thermal velocity of the precursor molecules given by

$$v_{th} = \sqrt{\frac{8RT}{\pi M}} \tag{4}$$

The transport and surface reaction of the precursor molecules are coupled through the internal boundary condition for Eq. (1), namely,

$$D(\nabla C \cdot \boldsymbol{n}) = \frac{1}{4} s_0 \beta_0 (1 - \theta) v_{th} C \tag{5}$$

where $\boldsymbol{n}$ is the normal vector of the surface.

In principle, the concentration field of the precursor should be solved in a time-dependent manner. However, the recent work by Yanguas-Gil and Elam [19] showed that, when the time scale for the evolution of the surface coverage (see Eq. (3)) is much longer than that of molecular diffusion (cf. Eq. (1)), the transient term in the diffusion transport equation can be neglected. Therefore, it is reasonable to treat the concentration field of the precursor as quasi-static under a given surface coverage and drop the transient term in Eq. (1). This simplification circumvents the need to resolve the unsteady precursor diffusion by brutal force and enables highly efficient simulation of the reactive transport processes of =ALD in porous electrodes, and is thus adopted in the present work.

Fig. 1. (a) Concept of the spatial ALD of porous electrodes. (b) A schematic of the pore-scale model of the reactive transport processes in porous electrodes during a half cycle of ALD.

2.1.2. One-dimensional mean-field model

Solving the above 3D pore-scale model in electrodes with complex microstructure is time consuming. Therefore, the 1D mean-field model has been widely used in the past. In this work, the effectiveness of the 1D mean-field model in predicting the ALD coating in porous electrodes is systematically examined by the 3D pore-scale model. Here, the 1D mean-field model is briefly introduced.

In the 1D mean-filed model, the porous electrodes are treated as a continuum characterized by a specific surface area $\bar{s}$. The transport of the precursor molecules in the electrode is modeled at the mean-field level using [19,20]

$$D_e \frac{\partial^2 C}{\partial x^2} = -\frac{1}{4}\bar{s}\beta_0(1-\theta)v_{th}C \tag{6}$$

where D_e is the effective diffusivity of the precursor molecule in the porous electrode; and $\bar{s}$ is the specific surface area (surface area per unit pore volume) [20]. The source term in Eq. (6) represents the reactions of precursor molecules with the active surface sites. Eq. (6), along with Eq. (3), forms the 1D mean-field model of ALD. Note that this 1D model is parameterized using only two parameters: $\bar{s}$ and D_e. D_e depends on the porosity of the electrode and is usually described using empirical models, e.g., the Bruggeman model.

2.2. Lattice Boltzmann method

At any time instant t_n, the quasi-static precursor concentration field C corresponding to the surface coverage distribution θ at this time instant is computed first. Specifically, the D3Q7 LB model is adopted to solve Equation (1) and the evolution equation of the distribution functions is

$$g_i(x + e_i\Delta t_f, t + \Delta t_f) - g_i(x, t_f) = -\frac{1}{\tau_g}(g_i(x, t_f) - g_i^{eq}(x, t_f)) \tag{7}$$

where g_i is the concentration distribution function along the i direction, t_f is the fictitious time, and Δt_f is the fictitious time step. g_i^{eq} is the corresponding equilibrium concentration distribution function

$$g_i^{eq} = \begin{cases} \omega_0 C, & i = 0 \\ (1 - \omega_0)/6 \times C, & i = 1, 2, \cdots 6 \end{cases} \tag{8}$$

where ω_0 is the weight parameter, which is set to be 1/7 in this study. In Eq. (7), e_i is the discrete velocity given by

$$e_i = \begin{bmatrix} 0 & 1 & -1 & 0 & 0 & 0 & 0 \\ 0 & 0 & 0 & 1 & -1 & 0 & 0 \\ 0 & 0 & 0 & 0 & 0 & 1 & -1 \end{bmatrix} \tag{9}$$

Through the Chapman-Enskog expansion (see Appendix A), one can find that Eq. (7) can recover to the macroscopic diffusion equation (Eq. (1)) and the relation between the gas diffusivity and relaxation time coefficient (τ_g) is

$$D = \frac{1}{3}(1 - \omega_0)(\tau_g - 0.5)\frac{\Delta x^2}{\Delta t_f} \tag{10}$$

and the macroscopic local concentration is determined by

$$C = \Sigma g_i \tag{11}$$

Unlike other numerical methods, the fundamental variables are the distribution functions in the LB framework. Therefore, boundary conditions based on the distribution functions are required for LB simulations. When precursor molecules collide with solid surfaces inside the porous media, they can react with the active surface sites. For each reactive surface boundary, the unknown distribution function can be calculated from the surface flux. For example, the unknown distribution function g_1 along the positive x direction can be given by [30,33]

$$\frac{\Delta x}{\Delta t_f}(g_1 - g_3) = -D\frac{\partial C}{\partial x} = \frac{1}{4}\beta_0(1-\theta)v_{th}C \tag{12}$$

$$g_1 + g_3 = g_1^{eq} + g_3^{eq} = (1 - \omega_0)/3 \times C \tag{13}$$

Once the precursor concentration field is marched to convergence to obtain $C(t_n)$, the surface coverage θ on the solid surfaces in the electrode at time t_n is updated using

$$\theta(t_{n+1}) - \theta(t_n) = s_0\beta_0(1 - \theta_n)v_{th}C_n\Delta t_\theta/4 \tag{14}$$

where Δt_θ is the time step size. Note that the time marching step Δt_θ is independent of the fictitious time step size Δt_f in Eq. (7). With the updated surface coverage $\theta(t_{n+1})$, the corresponding quasi-static concentration field at time instant t_{n+1} is solved and the above process is repeated. The iteration is continued until the surface coverage on the solid surfaces in the porous electrode reaches the required saturation.

3. Reconstruction and characterization of porous electrodes

First, reconstruction algorithms are used to build the microstructure of porous electrodes. Two types of electrodes, i.e., one consisting of connected spherical particles and the other consisting of connected spherical pores, have been reconstructed. Four parameters are adopted to control the microstructure of these electrodes, including the porosity, particle or pore radius, overlap probability and overlap tolerance, among which the overlap tolerance determines the maximum overlapping volume of two connected particles or pores. For the detailed
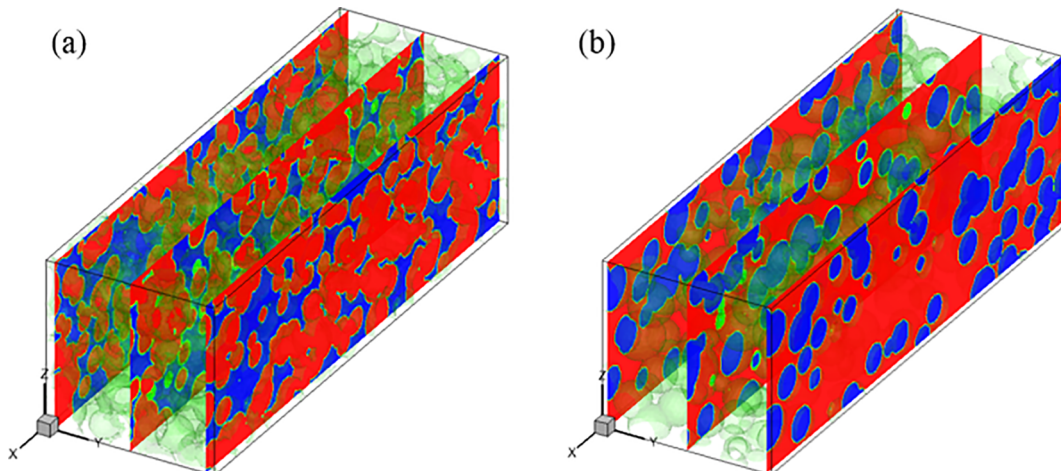

Fig. 2. Snapshots of reconstructed porous electrodes featuring connected spherical particles (a) and connected spherical pores (b). The red and blue color represent the solid and pore space, respectively. (For interpretation of the references to color in this figure legend, the reader is referred to the web version of this article.)

reconstruction algorithms, one can refer to Refs. [37,38]. Representative snapshots of porous electrodes reconstructed using connected spherical particles and connected spherical pores are shown in Fig. 2(a) and Fig. 2(b), respectively. For electrodes in Li-ion batteries, their porous electrodes are essentially made of packed particles, and thus the microstructure constructed using connected spherical particles are generally more reasonable than those featuring connected spherical pores. Therefore, most of our simulations are based on electrodes constructed using connected spherical particles (Section 5.1 and Section 5.2). Electrodes constructed using connected pores are only used to elucidate how pore connectivity, which is difficult to control in structures made of connected particles, affects ALD (Section 5.3). It is desirable to use a single method that can construct porous structures to resemble real electrodes rather than switching between model geometries. However, the development of such a method is highly non-trivial and beyond the scope of this study and the resources available to us. We hope that the effects of pore connectivity illustrated here will stimulate the development of methods for constructing porous structure from connected spheres with controlled pore connectivity.

Next, the porous electrodes reconstructed above are characterized in terms of their geometrical properties such as specific surface area, pore size distribution, and pore connectivity. In this study, the specific surface area is defined as the ratio of the total surface area to the total pore volume. In our LBM model, each pore node has 26 neighboring nodes (a $3 \times 3 \times 3$ cubic) located in thirteen directions. The pore width in each direction is first determined as the distance between the pore node and the nearest solid surface along this direction. Next, the pore size is obtained by averaging the pore width in all thirteen directions [39]. Fig. 3a shows the pore size distribution of representative electrodes used in Section 5.1. The pore connectivity is defined as the ratio of continuous percolation pores to the total pore cells, and is determined by a connected phase labeling algorithm [39] to distinguish connected and dead pores. Fig. 3b shows a snapshot of a reconstructed electrode with the connected and dead pores highlighted using different colors.

Finally, the homogenized transport properties of the reconstructed electrodes are computed. Specifically, because the effective diffusivity of the precursor molecules in the porous electrodes is of great importance for the precursor transport, it is determined numerically using the LBM. To this end, a concentration difference of the precursor gas is specified between the top surface ($x = 0$) and bottom surface ($x = L_x$) of the electrodes. At steady state, the induced diffusion flux is calculated to determine the effective diffusivity of the precursor through the electrode using Fick's law:

$$D_{\mathrm{e}} = \frac{\left(\int_0^{L_y} \int_0^{L_z} -D \frac{\partial C}{\partial x} \Big|_{x=L_x} dy dz \right) / L_y L_z}{(C_{\mathrm{in}} - C_{\mathrm{out}})/L_x} \tag{15}$$

where L_x, L_y, L_z are the length of the electrode along the x, y, and z direction, respectively. We note that the local Knudsen diffusivity D depends on the local pore diameter. In Eq. (15), the effective diffusivity D_e is averaged on the bulk volume. Another effective diffusivity can be defined as $D_e' = D_e/\varepsilon$, where ε is the porosity of the electrode. Thus, D_e' is averaged on the total pore volume [40]. The two effective diffusivities computed here will be used in the 1D mean-field model described in Section 2.2.

4. Code validation

To validate the LBM code developed for simulating the reactive transport processes in ALD, we use the code to study the coating of a straight cylindrical pore by ALD (see Fig. 4's inset). The pristine pore is initially free of precursor molecules. At $t = 0$, the concentration of the precursor at the pore entrance is set to that corresponding to the partial pressure of the precursor to initiate the coating. For this problem, Yanguas-Gil and Elam derived a semi-empirical analytical expression of the exposure time required to reach a target surface coverage θ at the bottom of the pore [19]:

$$t_c = \frac{1}{2} \frac{L^2}{D} \frac{1}{\gamma} \left(1 - \frac{\ln(1-\theta)}{\alpha} \right) \tag{16}$$

where L is the pore length; θ is the coverage fraction of the solid surface at the bottom of the pore ($x = L_x$ in Fig. 4's inset). α is the Damkohler number representing the ratio of the reaction rate and diffusion rate, and it is defined as

$$\alpha = \frac{1}{4} L^2 \bar{s} \frac{v_{th}}{D} \beta_0 \tag{17}$$

γ is the number of precursor molecules per unit surface site, and it is defined as

$$\gamma = n_0 s_0 / \bar{s} \tag{18}$$

where n_0 is the number density of the precursor molecule at the pore entrance and it is related to the partial pressure of the precursor p_P by $n_0 = p_P/k_B T$ (k_B is the Boltzmann constant). Fig. 4(a) shows the required exposure time for achieving a surface coverage of $\theta = 0.9$ at the pore's bottom surface obtained using our code. Here, the pore diameter d is
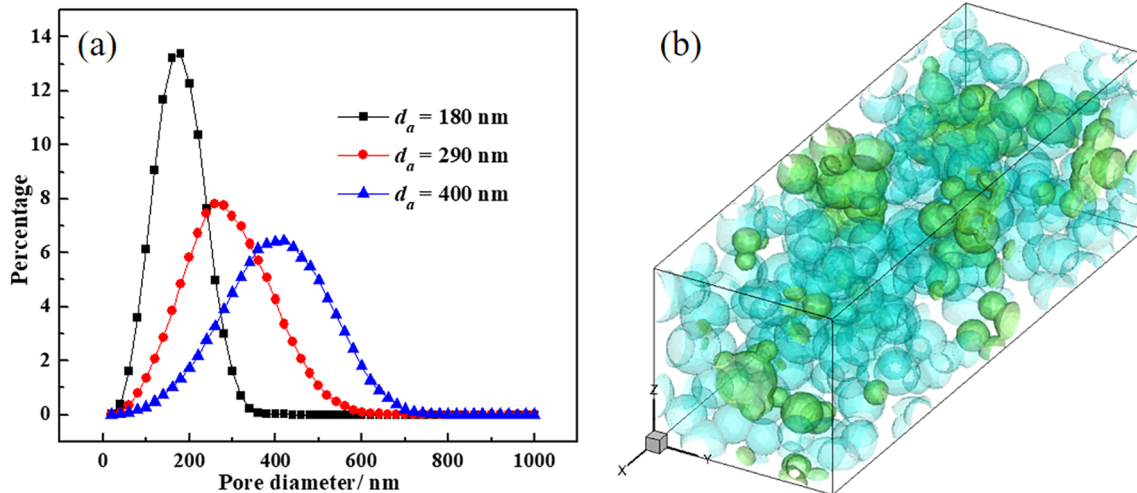

Fig. 3. (a) The pore size distribution of the reconstructed porous electrodes with different average pore size. (b) A snapshot of a representative porous electrode consisted of connected spherical pores. The blue and green color represent the connected and "dead" pores, respectively. (For interpretation of the references to color in this figure legend, the reader is referred to the web version of this article.)
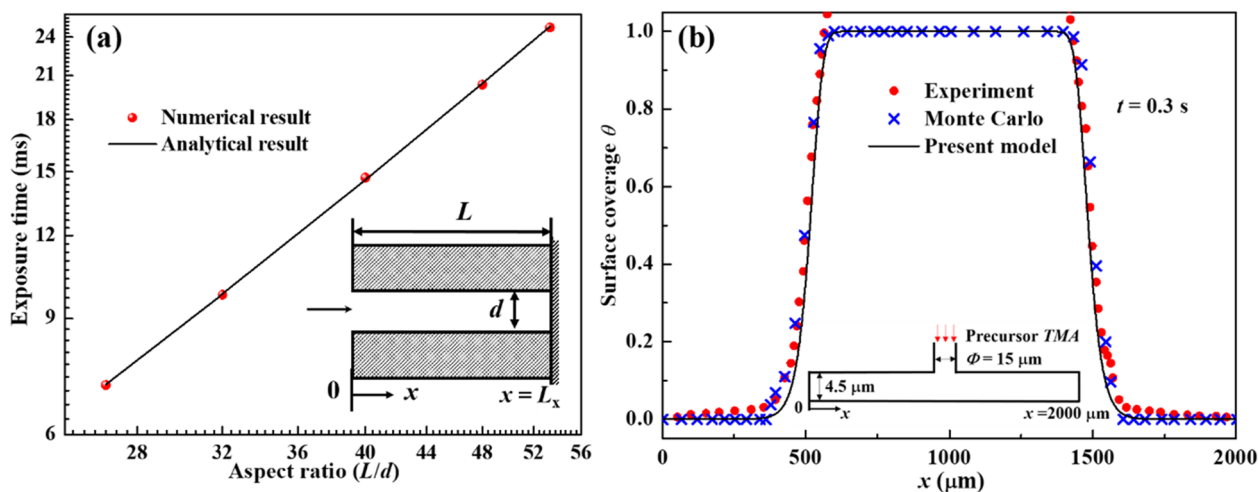
Fig. 4. Validation of present numerical model. (a) Validation against analytical predictions of the exposure time of straight pores with different aspect ratios (L/d). The target surface coverage at the pore bottom is taken as $\theta = 0.9$. (b) Comparison of the surface coverages of ALD coating on a high-aspect-ratio cavity obtained by experiments [42], the Monto Carlo simulation [42], and the present model.

fixed to be 150 nm, and the length L is varied from 4 μm to 8 μm. The initial sticking coefficient β_0 is set to be 0.01 [41], $s_0 = 10^{-19}\,\text{m}^2$ [19], and the inlet pressure is 1 Torr [11]. The very good agreement between the computed exposure time and that given by Eq. (16) validates the accuracy of the present method.

Next, the present model is validated against the experiment data and Monte Carlo simulation conducted by Schwille et al. [42]. The surface coverage profile of ALD coating on a high-aspect-ratio cavity is obtained. The lateral dimension of the cavity is 2000 μm, and its height is 4.5 μm. The precursor trimethylaluminum (TMA) is injected from the central hole with a diameter 15 μm. The comparison of the surface coverage profiles at $t = 0.3\,\text{s}$ is presented in Fig. 4 (b). The inlet pressure is 0.3 mbar, and initial sticking coefficient $\beta_0 = 0.02$, as those in Ref. [42]. In the center of the domain, more than a monolayer of the material can be deposited due to the inevitable chemical vapor deposition. Thus, the surface coverage (normalized film thickness) obtained by the experiment data can be larger than 1. The very good agreement between our model predictions and the previous experimental data and numerical predictions supports the validity of our model and simulation codes.

5. Results and discussions

In this study, we only consider one of the half cycles in an ALD cycle. The trimethylaluminum (TMA) is selected as the precursor in this half cycle. The transport properties of the TMA molecule and other operating conditions are shown in Table 1. The reported initial sticking coefficient (β_0) for TMA ranging from 0.001 to 1 in the literature [18,41,43]. In this study, the sticking coefficient ranging from 0.001 to 0.1 is chosen to study how the reactivity of precursor molecules affects ALD. In most cases, the initial sticking coefficient β_0 is set to be 0.01, as reported in Ref. [43]. For the three-dimensional pore-scale model, the porous electrode spans 2 μm × 2 μm in the lateral direction and 6 μm in the depth direction. The periodical boundary condition is prescribed in the lateral direction. The precursor concentration on the top electrode surface ($x = 0$ in Fig. 1b) is set to that defined by the precursor pressure (see Table 1). A no-flux boundary condition is prescribed on the bottom electrode surface ($x = L_x$ in Fig. 1b). The electrode is partitioned into a 300 × 100 × 100 grid with a uniform grid spacing of 20 nm. The lateral size of the computational domain (y- and z- direction) is sufficiently large since the key characteristic parameters (pore size, connectivity and effective diffusivity) only deviate slightly from those calculated in a 300 × 200 × 200 domain.

5.1. Effects of pore size

To investigate the effects of pore size on the coating process of ALD, three electrodes with different average pore sizes are reconstructed. The pore size distributions of these electrodes are shown in Fig. 3(a). The detailed microstructure information and the effective diffusivities of the precursor molecules in these electrodes are characterized using the method described in Section 4 and the results are summarized in Table 2. The electrode with a smaller average pore size has a larger specific surface area and a smaller effective diffusivity. The pore connectivity in each of the reconstructed electrodes is nearly 1.0, indicating that the pores in these electrodes are well connected.

Under the operating conditions listed in Table 1, the ALD of the reconstructed electrodes are simulated by solving the 3D pore-scale model and the 1D mean-field model. The latter model is parameterized using the specific surface areas and effective diffusivities listed in Table 2. Fig. 5 compares the evolution of the surface coverage profile along the depth direction of the electrodes predicted by the two models (for the 3D pore-scale model, the surface coverage profile is the cross-section averaged result). We observe that, when the 1D mean-field model is parameterized using the pore volume-based effective diffusivity $D_e^{'}$, it can predict the averaged coating process rather well. The 1D model based on the electrode volume-based effective diffusivity D_e significantly underestimates the propagation of the surface coverage profile through the electrodes. The effectiveness of the 1D model is also supported by a detailed look at the evolution of the surface coverage at the bottom of the electrode. For example, in electrode I, the 3D pore-scale model predicts that a 90% of surface coverage is achieved at 11.18 ms while the 1D model parameterized using $D_e^{'}$ predicts 10.70 ms is required.

Fig. 5 shows that, as the average pore size in the electrode decreases, the front of the surface coverage profile becomes steeper and its propagation toward the electrode's interior becomes slower. The latter

Table 1
Physical properties of the precursor and simulation parameters.

Parameter	Value
Temperature of the precursor, T_p	400 K
Molecular mass of the precursor molecule, M	72.9 g/mol
Precursor pressure, Pp	1 Torr (133.29 Pa) [11]
Sticking coefficient β_0	0.01 [41,43]
Area of a surface site, s_0	$10^{-19}\,\text{m}^2$ [19]
Gas constant, R	8.314 J/(mol·K)

Table 2
Geometrical and transport properties of the reconstructed porous electrodes.

Parameters	Electrode I	Electrode II	Electrode III
Average pore diameter, d_a	400 nm	290 nm	180 nm
Porosity, ε	0.3	0.3	0.3
Pore connectivity	99.99%	99.98%	99.97%
Specific surface area, $\bar{s}$	$2.08 \times 10^7\,\mathrm{m}^{-1}$	$2.97 \times 10^7\,\mathrm{m}^{-1}$	$4.77 \times 10^7\,\mathrm{m}^{-1}$
Bulk volume averaged diffusivity, D_e	$5.32 \times 10^{-6}\,\mathrm{m}^2/\mathrm{s}$	$3.52 \times 10^{-6}\,\mathrm{m}^2/\mathrm{s}$	$1.94 \times 10^{-6}\,\mathrm{m}^2/\mathrm{s}$
Pore volume-averaged diffusivity, $D_e^{'}$	$1.73 \times 10^{-5}\,\mathrm{m}^2/\mathrm{s}$	$1.17 \times 10^{-5}\,\mathrm{m}^2/\mathrm{s}$	$6.47 \times 10^{-6}\,\mathrm{m}^2/\mathrm{s}$

results in a longer required exposure time for the bottom of the electrodes to be coated. For example, the exposure times required to achieve a 90% coverage of the bottom surface are 11.18 ms, 21.88 ms and 56.89 ms for the electrodes with an average pore diameter of 400 nm, 290 nm and 180 nm, respectively. These phenomena can be understood using the 1D mean-field model. According to the definitions of α and γ in Eqs. ((17)–(18)), we have $\alpha_1 = 17.97$, $\gamma_1 = 1.16 \times 10^{-4}$ for electrode I ($d_a = 400$ nm), $\alpha_2 = 38.80$, $\gamma_2 = 8.13 \times 10^{-5}$ for electrode II ($d_a = 290$ nm), and $\alpha_3 = 113.15$, $\gamma_3 = 5.06 \times 10^{-5}$ for electrode III ($d_a = 180$ nm). For all electrodes, $\alpha \gg 1$, i.e., the reaction rate of the precursor molecules is much larger than their diffusion rate, which means the process is diffusion-limited. As such, precursor molecules will be captured by the reactive surface before they diffuse deep into electrodes. The larger α in electrode III than in other electrodes explains why the drop of the surface coverage value is sharpest along the depth direction of electrode III. For all electrodes, $\gamma \ll 1$, i.e., the number of the precursor molecules in the pore volume is much lower than the reactive surface sites on the pore surface. Sine γ is smallest in electrode III and the diffusion of precursor molecules is slowest in this electrode due to its smaller pore size (cf. Eq. (2)), the longest exposure time is needed for the bottom surface of this electrode to achieve the same surface coverage as in other electrodes.

5.2. Effects of secondary pores

The pores in many porous electrodes exhibit a multimodal size distribution, e.g., in addition to the main pores formed between particles in the electrodes, secondary pores with smaller sizes are also prevalent. These secondary pores can come from the cracks within large particles and/or the pores formed between very small particles in the electrodes. To investigate effects of the secondary pores on ALD, we reconstructed three electrodes as shown in Fig. 6. The first electrode is built using the method described in Section 3. It has a porosity of 0.2 and a unimodal pore size distribution (see Fig. 7). Two other electrodes are reconstructed from this electrode using the improved quartet structure generation set method [44]. Specifically, pore seeds are first

distributed at pore-electrode interfaces based on a distribution probability that ensures the connectivity between the secondary and main pores. These seeds then grow inside the electrodes to neighboring cells until the electrode porosity reaches 0.3. By adjusting the growth probability in each direction, different alignment of the secondary pores can be achieved. In real electrodes, the secondary pores are randomly oriented. Here, we assess two limiting cases (they are aligned parallel and normal to the overall direction of the precursor gas transport, i.e., the long axis of the pores is aligned in the *x*- and *y*-directions, see Fig. 6b-c). Examining the coating process under these limiting conditions helps clarify to what extent the orientation of secondary pores affects the coating behavior.

Fig. 7 compares the three electrodes' pore size distribution. The bimodal pore size distributions of the modified electrodes suggest that these electrodes feature main pores with an average diameter of ~250 nm and secondary pores with an average diameter of ~90 nm. The pore connectivity in the electrodes shown in Fig. 6a, b, and c are found to be 99.85%, 99.73% and 99.77%, respectively, indicating that both main pores and secondary pores are well connected.

The ALD of the three electrodes shown in Fig. 6 is simulated under the operating conditions shown in Table 1. Fig. 8 shows the distribution of the surface coverage profile across the three electrodes at a representative time instant. We observe that the introduction of the secondary pores slows down the movement of the coating front toward the interior of the electrode, especially when these pores are aligned in the *y*-direction (i.e., normal to the direction of precursor transport). These trends are also consistent with the observation that the exposure times required to reach a 90% surface coverage on the bottom of the electrodes shown in Fig. 6(a), (b) and (c) are 53.0 ms, 57.82 ms and 67.59 ms, respectively.

The slowdown of the coating front upon the introduction of the secondary pores can be explained as follows. As secondary pores are added, the electrodes' specific surface area increases. Because the reactive surface sites serve as sinks for the precursor molecules, increasing the specific surface area requires more precursor molecules to be transported into electrodes' interior during ALD. In the diffusion-
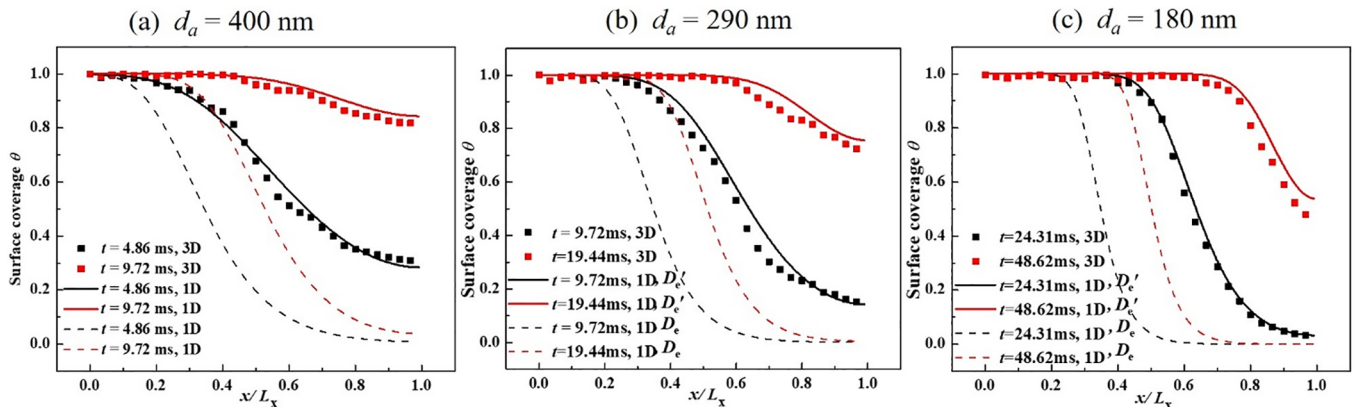

(a) $d_a = 400$ nm   (b) $d_a = 290$ nm   (c) $d_a = 180$ nm

Fig. 5. Comparisons of the surface coverage profiles along the depth direction obtained by 3D pore-scale model and 1D mean-field model in electrodes with an average pore size of $d_a = 400$ nm (a), $d_a = 290$ nm (b), and $d_a = 180$ nm (c).
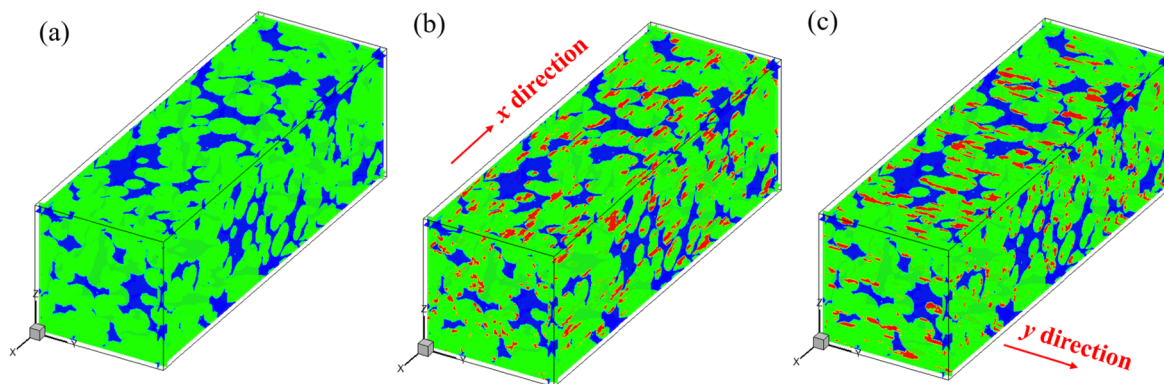
Fig. 6. Snapshots of the original electrode (a) and its two modifications (b-c). In (b) and (c), secondary pores aligned along the *x*- and *y*-directions of the electrode are introduced. The green color represents solids. The blue and red color represents the original pores and the secondary pores introduced later. (For interpretation of the references to color in this figure legend, the reader is referred to the web version of this article.)
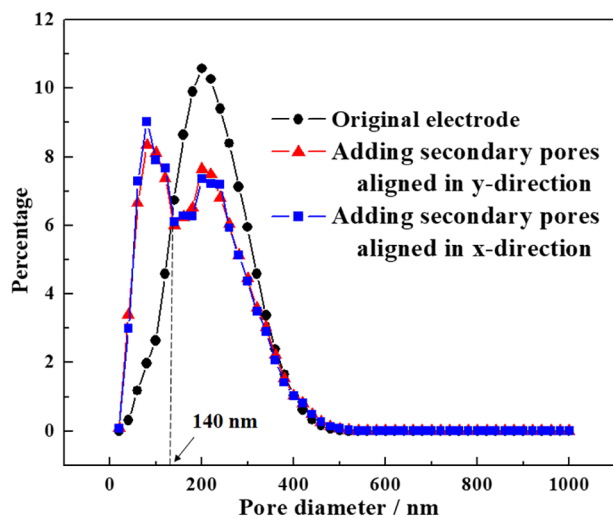

Fig. 7. The pore size distribution of the reconstructed porous electrodes shown in Fig. 6.

limited ALD studied here ($\alpha \gg 1$), the coating front is relatively sharp and few precursor molecules diffuse forward until the reactive surface sites behind them are exhausted. Adding small secondary pores into an electrode tends to slow down the transport of the precursor toward the electrode interior and thus slows down the coating front. This effect is akin to the fact that, as the specific surface area $\bar{s}$ increases, the γ in Eq. (18) decreases, and thus the exposure time t_c predicted by Eq. (16) increases.

Introducing secondary pores can affect the movement of the coating front during electrode coating in two ways. First, it leads to an increase of the surface area that serves as a sink to the precursor molecules and thus tends to slow down the movement of the coating. Second, to a lesser extent, secondary pores can facilitate the diffusion of precursor molecules through an electrode, which tends to accelerate the movement of the coating front. The latter effect is more pronounced when the secondary pores are aligned in the direction of the diffusion of precursor molecules (in our study, the *x*-direction). This explains why the slowdown of the coating front is less significant when the secondary pores are aligned in the *x*-direction than when they are aligned in the *y*-direction as shown in Fig. 8a.

We also assess the effectiveness of the 1D mean-field model for electrodes featuring secondary pores. To this end, we compute the specific surface area and effective diffusivity of the electrode shown in Fig. 6c and use them in the model given by Eq. (6). Fig. 9 shows that, for the two Damkohler numbers α studied here, the 1D mean-field model works rather well even when the electrode features a bimodal pore size distribution. Although the 1D mean-field model can predict the *average* surface coverage profile in the electrode's depth direction, this model does not provide insight into the potential difference of the coating behavior of pores with different sizes at the same depth in the electrode.
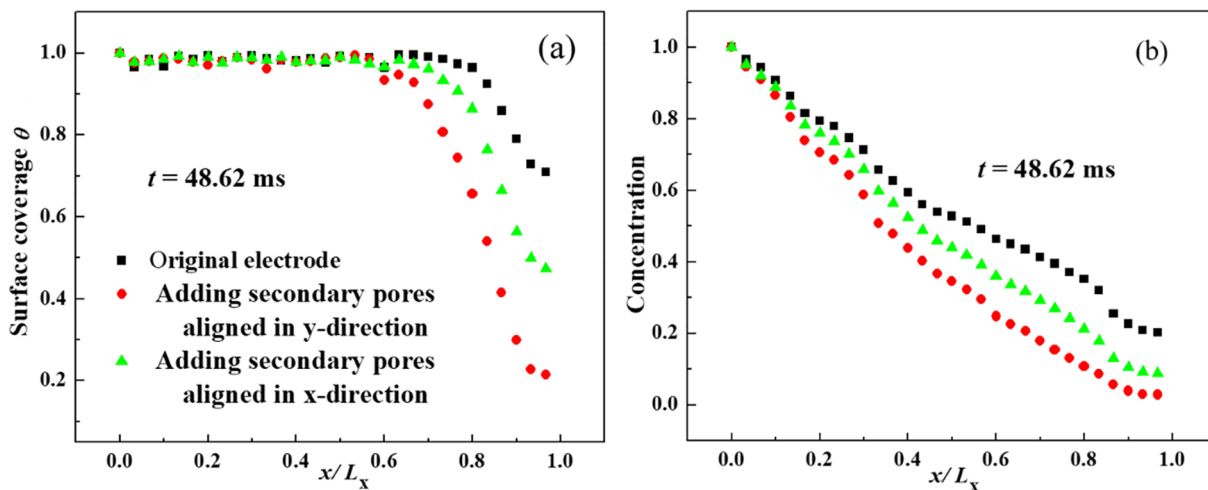

Fig. 8. Comparisons of the surface coverage profile (a) and the precursor concentration profile (b) along the depth direction of electrodes with different micro-structures.
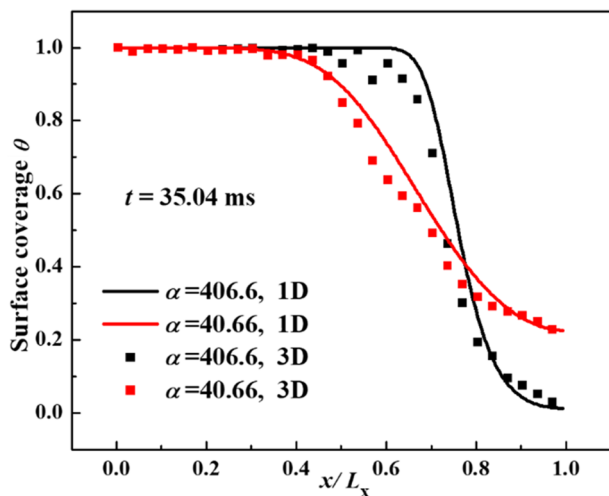
Fig. 9. Comparisons of the cross section-averaged surface coverage profiles predicted by the 3D pore-scale models and the 1D mean-field model at different values of Damkohler numbers α.

To examine this potential difference, we divided the pores in the electrode shown in Fig. 6c into "main" pores and "secondary" pores with diameter larger and smaller than 140 nm, respectively. Fig. 10 shows the time evolution of the surface coverage in the main and secondary pores at three different depths of the electrode computed by our 3D pore-scale model (the averaged Damkohler number α in the electrode is 406.6 here, and reducing it to 40.66 leads to qualitatively similar results). We observe that, at the same depth, the smaller secondary pores take a longer time to be fully saturated than the larger main pores. This observation is true for all the electrode depths examined. These results are consistent with the fact that smaller pores have a higher local specific surface area and lower local precursor diffusion coefficient.

5.3. Effects of pore connectivity

The pores inside real electrodes are sometimes poorly connected. The pores in electrodes formed by connected spherical particles studied in the previous sections are well connected, with the pore connectivity approaching 1.0. To study the effects of pore connectivity on the ALD process, additional electrodes are built using the connected spherical pores method by adjusting the overlap probability parameter in the reconstruction algorithm [38]. A reconstructed electrode with abundant dead-end pores is shown in Fig. 11(a), in which the pore connectivity is 80.6%. Next, connecting paths are introduced to link the dead pores and originally connected pores to form a porous electrode with a pore connectivity 99.62%, as shown in Fig. 11(b). For

convenience, the electrode with abundant dead pores (Fig. 11(a)) is labeled as "M1" and the electrode with poorly connected pores (Fig. 11(b)) is labeled as "M2". The porosities of M1 and M2 electrode are both 0.3. In electrode M2, the pores are divided into two groups: the well-connected pores and the poorly-connected pores, which correspond to the connected pores and dead pores in the M1 electrode, respectively.

The ALD of the two electrodes shown in Fig. 11 is simulated under the operating conditions shown in Table 1. Fig. 12 (a) shows the cross section-averaged surface coverage profiles in the depth direction of electrodes M1 and M2 at a representative time. For electrode M1, the surface coverage, when averaged over all pores, can be much less than 1.0 behind the coating front since the dead pores are never coated. When only connected pores are considered, the surface coverage profile becomes similar to those shown in Figs. 5 and 9. For electrode M2, the coating rates averaged over all pores is considerably slower than that of the connected pores in electrode M1. Indeed, the exposure times required to cover 90% of the bottom surface are 111.8 ms and 136.1 ms for electrodes M1 and M2, respectively. The slower average coating speed for all pores in electrode M2 is caused partly by the fact that the poorly connected pores in this electrode is coated slowly due to the inefficient transport of precursor molecules to these pores. In addition, Fig. 12(a) shows that the coating of the well-connected pores in electrode M2 is also slower than the connected pores in electrode M1. This phenomenon is caused by the fact that the poorly-connected pores in M2 serve as a significant sink to the precursor molecules due to their large specific surface area, depleting the precursor molecules near them and thus slowing down the propagation of precursors toward the well-connected pores in the deep interior of the electrode.

Fig. 12(b) shows a representative cross section-averaged surface coverage profiles along the electrode depth direction predicted by the 3D pore-scale model and the 1D mean-field model. For electrode M1, the 1D model parameterized using the effective diffusivity and specific surface areas discussed in Section 5.1 cannot predict the surface coverage profile well because the dead pores in the electrode cannot be coated and their surfaces are included in the calculation of the specific surface area. To remove the dead pores' contributions to the specific surface area and the porosity of the electrode, a new specific surface area $\bar{s}_{con} = S_{con}/V_{con}$ (S_{con} and V_{con} are the total surface area and volume of the connected pores) and a new effective diffusivity $D'_{e,con} = D_e/\varepsilon_{con} = D_e'\varepsilon/\varepsilon_{con}$ [40] (ε_{con} is the effective porosity $\varepsilon_{con} = V_{con}/V$, where V is the bulk volume of the electrode) are defined. Physically, $D'_{e,con}$ accounts for the fact that precursor molecules can only diffuse through connected pores. When $\bar{s}_{con}$ and $D'_{e,con}$ are used in the 1D mean-field model, the agreement between the 1D model and the pore-scale model improves (see Fig. 12(b)). For electrode M2, the 1D model captures the surface coverage at some positions reasonably well (e.g., near the bottom surface of the electrode) but performs poorly at other locations. For example, it overestimates the surface coverage in the
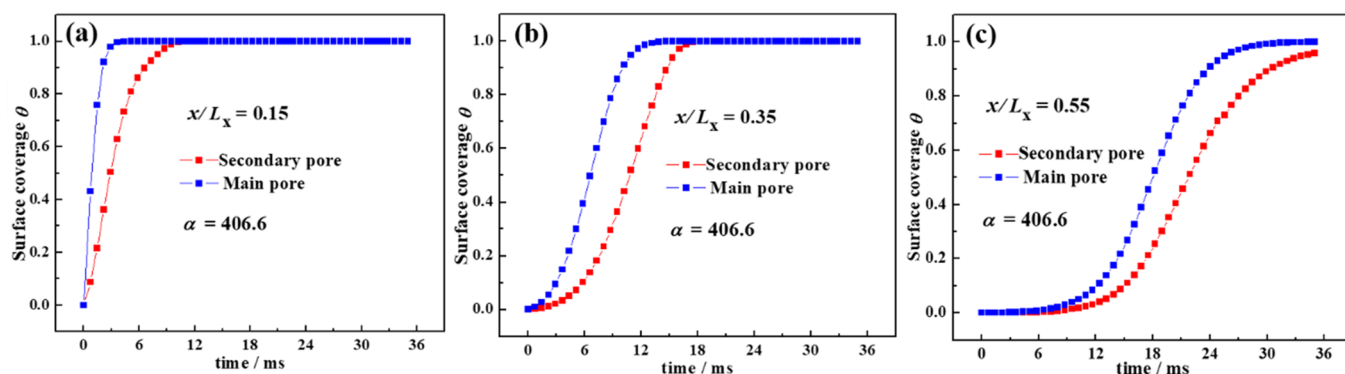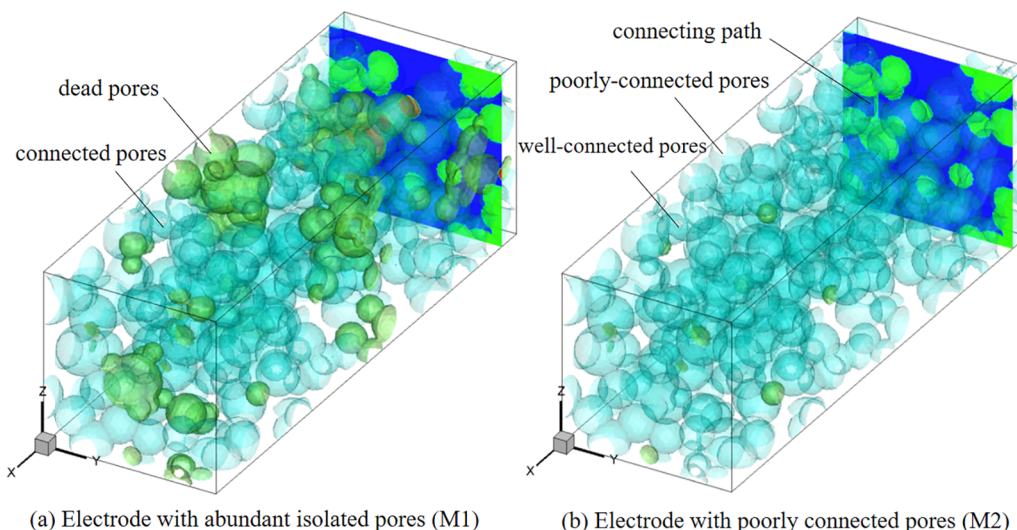

Fig. 10. The time evolution of the surface coverage in the main and secondary pores located at a depth of $x/L_x = 0.15$ (a), $x/L_x = 0.35$ (b), and $x/L_x = 0.55$ (c) in the electrode shown in Fig. 6b.

(a) Electrode with abundant isolated pores (M1)   (b) Electrode with poorly connected pores (M2)

Fig. 11. Snapshots of two reconstructed electrodes with abundant dead pores (a) and poorly connected pores (b).
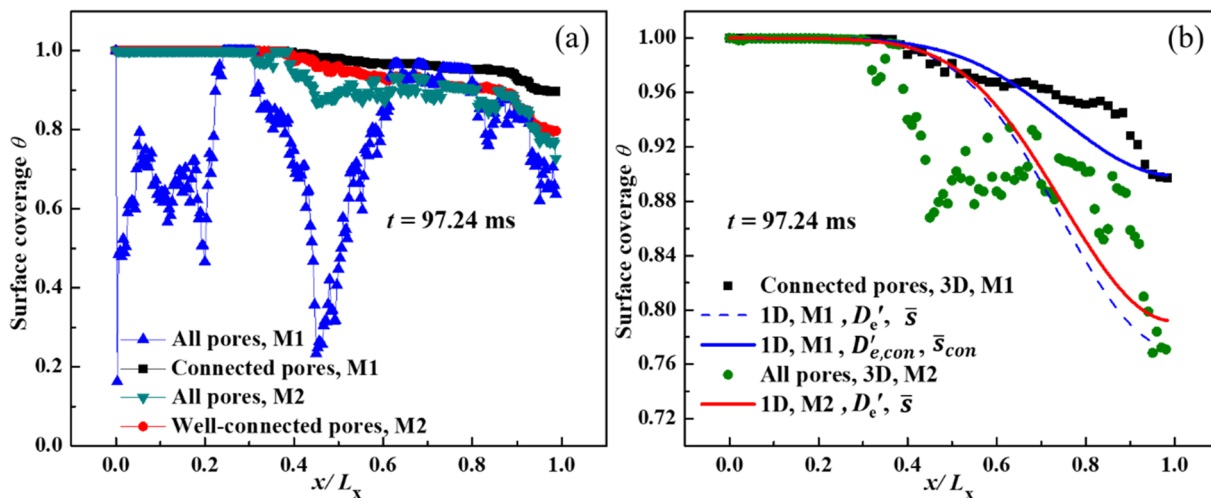

Fig. 12. The cross section-averaged surface coverage profiles in the depth direction of electrodes with different pore connectivity computed using the 3D pore-scale model (a) and their comparisons with the predictions by the 1D mean-field model (b).

region $0.4 < x/L_x < 0.6$, which is largely caused by the large population of poorly connected pores in this region that are hard to reach by the precursor molecules.

To further delineate the difference in the coating of the well- and poorly-connected pores in the M2 electrode, we examine the time evolution of the surface coverages of these pores at electrode depths of
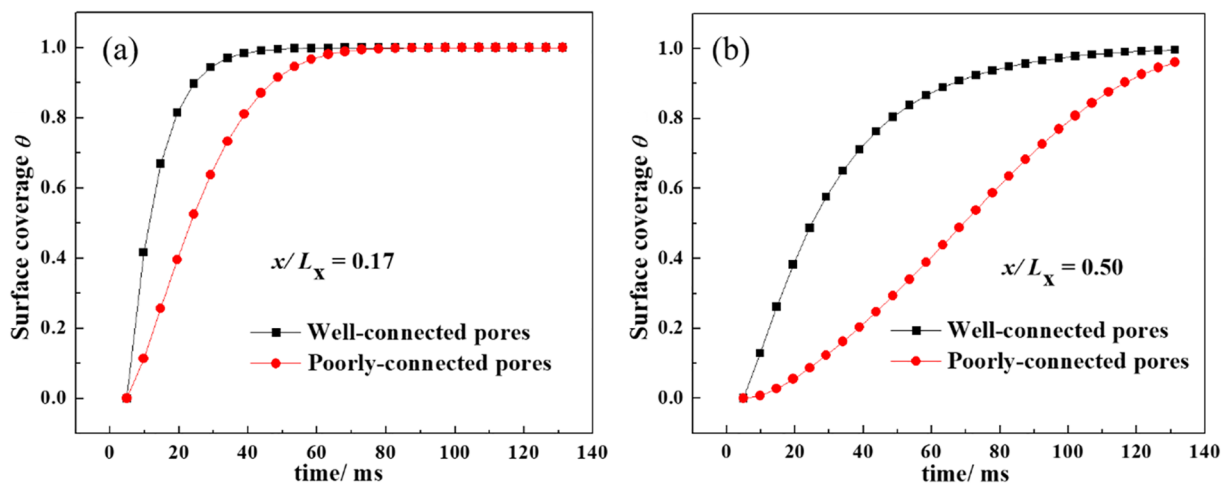

Fig. 13. Time evolution of the surface coverage of different pores at the various cross-sections in the electrode M2: $x/L_x = 0.17$ (a) and $x/L_x = 0.5$ (b).
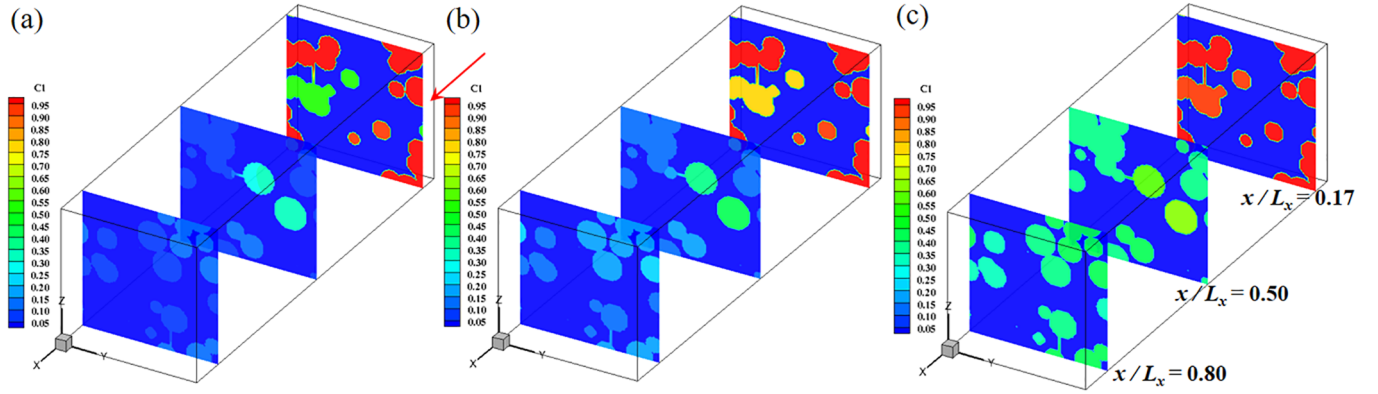
Fig. 14. Concentration distributions of precursors in the porous electrodes at the moment $t = 24.31$ ms (a), $t = 48.62$ ms (b), and $t = 97.24$ ms (c).

$x/L_x = 0.17$ and 0.50 (see Fig. 13). At the same depth, the growth of the surface coverage of the poorly-connected pores generally lags behind that of the well-connected pores, but with sufficient exposure time, the poorly-connected pores are eventually fully coated. The slower coating of the poorly connected pores is caused by the greater mass transfer resistance for precursors to diffuse into the poorly-connected pores than that into the well-connected pores. The larger mass transfer resistance is also manifested in the distribution of precursor concentrations for different pores at the same cross-section. As shown in Fig. 14, there often exists a distinct concentration difference between the well-connected pores and poorly-connected pores at the same cross section. As the exposure time increases, the reactive surfaces of all pores are gradually deactivated and no longer consume precursor molecules. As a result, the concentration difference inside the well- and poorly-connected pores becomes similar.

6. Conclusions

The 3D pore-scale reactive transport processes of ALD in the reconstructed electrodes are solved using LBM to systematically examine how ALD is affected by the pore size, existence of secondary pores, and pore connectivity. It was found that, when the ALD operates in the diffusion-limited regime, the coating front becomes steeper and its propagation into electrode's interior slows down as the pore size becomes smaller. Specifically, the required exposure time is 11.18 ms for electrodes with an average pore diameter of 400 nm while 56.89 ms for that of 180 nm. The presence of small secondary pores in electrodes, which leads to a multimodal pore size distribution, slows down the speed of the coating front and increases the exposure time needed (changed from 53.0 to 67.59 ms) to achieve full surface coverage of the pores inside the electrode. The existence of poorly-connected pores inside electrodes can significantly slow down the coating speed

(changed from 111.8 to 136.1 ms) and lead to a wide range of surface coverage among pores at the same depth within the electrode. These phenomena are the combined effects of the mass diffusion within the porous electrode and the consumption of precursor molecules by the reactive surfaces of the connected pores in the electrodes.

Using the 3D pore-scale simulation results, the effectiveness of the 1D mean-field model in predicting the ALD coating in porous electrodes is systematically examined. When the pores in electrodes are well connected and the pore size distribution is relatively narrow, the 1D model can accurately predict the evolution of the surface coverage profile and the exposure time needed to achieve full surface coverage if the 1D model is suitably parameterized. In particular, the effective diffusivity of the precursor molecules in the electrode should be computed based on the electrode's microstructure (i.e., the tortuosity of the mass transport path should be taken into account) and the effective diffusivity should be based on the connected pores (effective porosity). When the electrode features abundant secondary pores, the 1D mean-field model can still predict the *average* surface coverage profile reasonably well although it neglects the dispersion of the surface coverage of pores at the same electrode depth. In electrodes with a large number of poorly-connected pores, the 1D mean-field model can no longer accurately predict the evolution of the surface coverage profile (and thus the minimal exposure time for achieving desired surface coverage) in the electrodes.

Appendix A. Chapman-Enskog Expansion

Eq. (7) can be expanded by the Tylor series:

$$D_i g_i + \frac{\Delta t_f}{2} D_i^2 g_i = -\frac{1}{\tau_g \Delta t_f}(g_i - g_i^{eq}) \tag{A.1}$$

where

$$D_i = \frac{\partial}{\partial t} + e_i \cdot \nabla \tag{A.2}$$

The distribution function can be expanded as a series of functions with a small parameter ϵ

$$g_i = g_i^{(0)} + \epsilon g_i^{(1)} + \epsilon^2 g_i^{(2)} + \cdots \tag{A.3}$$

$$\partial_{x_i} = \epsilon \partial_{x_i} \tag{A.4}$$

$$\partial_t = \epsilon^2 \partial_t \tag{A.5}$$

where $g_i^{(0)}$ equals g_i^{eq}. From Eq. (11) and Eq. (A.3), we can derive that the non-equilibrium parts $g_i^{(1)}$, $g_i^{(2)}$ are summed to be zero

$$\sum_i g_i^{(1)} = 0, \quad \sum_i g_i^{(2)} = 0 \tag{A.6}$$

Substituting Eqs. (A.3–5) into Eq. (A.1) and then equating coefficients of the same order ϵ yield the following relations [29]

$$\epsilon^1: e_{i\alpha} \frac{\partial f_i^{(0)}}{\partial x_\alpha} = -\frac{1}{\tau_g \Delta t_f} g_i^{(1)} \tag{A.7}$$

$$\epsilon^2: \frac{\partial g_i^{(0)}}{\partial t} + e_{i\alpha} \frac{\partial g_i^{(1)}}{\partial x_\alpha} + \frac{\Delta t_f}{2} e_{i\alpha} e_{i\beta} \frac{\partial^2 g_i^{(0)}}{\partial x_\alpha \partial x_\beta} = -\frac{1}{\tau_g \Delta t_f} g_i^{(2)} \tag{A.8}$$

Taking the deviation of Eq. (A.7) yields:

$$\frac{\partial g_i^{(1)}}{\partial x_\alpha} = -e_{i\beta} \frac{\partial^2 g_i^{(0)}}{\partial x_\alpha \partial x_\beta} \tau_g \Delta t_f \tag{A.9}$$

Thus, the left side of Eq. (A.8) can be rewritten as follows:

$$\frac{\partial g_i^{(0)}}{\partial t} + \tau_g \Delta t_f (\frac{1}{2\tau_g} - 1) e_{i\alpha} e_{i\beta} \frac{\partial^2 g_i^{(0)}}{\partial x_\alpha \partial x_\beta} = -\frac{1}{\tau_g \Delta t_f} g_i^{(2)} \tag{A.10}$$

Summing Eq. (A.10) over all the directions to recover the macroscopic diffusion equation

$$\frac{\partial T}{\partial t} + \tau_g \Delta t_f (\frac{1}{2\tau_g} - 1) \zeta c^2 \frac{\partial^2 T}{\partial^2 x_\alpha} = 0 \tag{A.11}$$

To obtain Eq. (A.11), the following relation is used

$$\sum_i e_{i\alpha} e_{i\beta} \omega_i = \zeta c^2 \delta_{\alpha\beta} \tag{A.12}$$

where $\zeta = (1 - \omega_0)/3$ and $c = \Delta x / \Delta t_f$. By the comparison between macroscopic diffusion equation (see Eq. (1)) and Eq. (A.11), we can find:

$$D = \frac{1}{3} (1 - \omega_0)(\tau_g - 0.5) \frac{\Delta x^2}{\Delta t_f} \tag{A.13}$$

References

[1] S.M. George, Atomic layer deposition: an overview, Chem. Rev. 110 (2009) 111–131.

[2] P.S. Maydannik, T.O. Kääriäinen, D.C. Cameron, An atomic layer deposition process for moving flexible substrates, Chem. Eng. J. 171 (2011) 345–349.

[3] K.H. Park, G.D. Han, K.C. Neoh, T.S. Kim, J.H. Shim, H.D. Park, Antibacterial activity of the thin ZnO film formed by atomic layer deposition under UV-A light, Chem. Eng. J. 328 (2017) 988–996.

[4] S. Hy, Y.H. Chen, H.M. Cheng, C.J. Pan, J.H. Cheng, J. Rick, B.J. Hwang, Stabilizing nanosized Si anodes with the synergetic usage of atomic layer deposition and electrolyte additives for Li-ion batteries, ACS Appl. Mater. Inter. 7 (2015) 13801–13807.

[5] Y. He, X. Yu, Y. Wang, H. Li, X. Huang, Alumina-coated patterned amorphous silicon as the anode for a lithium-ion battery with high Coulombic efficiency, Adv. Mater. 23 (2011) 4938–4941.

[6] P. Poodt, A. Lankhorst, F. Roozeboom, K. Spee, D. Maas, A. Vermeer, High-speed spatial atomic-layer deposition of aluminum oxide layers for solar cell passivation, Adv. Mater. 22 (2010) 3564–3567.

[7] D.J. Higgs, J.W. DuMont, K. Sharma, S.M. George, Spatial molecular layer deposition of polyamide thin films on flexible polymer substrates using a rotating cylinder reactor, J. Vac. Sci. Technol. A 36 (2018) 01A117.

[8] E. Granneman, P. Fischer, D. Pierreux, H. Terhorst, P. Zagwijn, Batch ALD: characteristics, comparison with single wafer ALD, and examples, Surf. Coat. Tech. 201 (2007) 8899–8907.

[9] Z. Deng, W. He, C. Duan, R. Chen, B. Shan, Mechanistic modeling study on process optimization and precursor utilization with atmospheric spatial atomic layer deposition, J. Vac. Sci. Technol. A 34 (2016) 01A108.

[10] D. Pan, L. Ma, Y. Xie, T.C. Jen, C. Yuan, On the physical and chemical details of alumina atomic layer deposition: a combined experimental and numerical approach, J. Vac. Sci. Technol. A 33 (2015) 021511.

[11] Y. Xie, L. Ma, D. Pan, C. Yuan, Mechanistic modeling of atomic layer deposition of alumina process with detailed surface chemical kinetics, Chem. Eng. J. 259 (2015) 213–220.

[12] P. Poodt, A. Mameli, J. Schulpen, W. Kessels, F. Roozeboom, Effect of reactor pressure on the conformal coating inside porous substrates by atomic layer deposition, J. Vac. Sci. Technol. A 35 (2017) 021502.

[13] M. Ylilammi, O.M. Ylivaara, R.L. Puurunen, Modeling growth kinetics of thin films made by atomic layer deposition in lateral high-aspect-ratio structures, J. Appl. Phys. 123 (2018) 205301.

[14] T. Cale, G. Raupp, Free molecular transport and deposition in cylindrical features, J. Vac. Sci. Technol. B 8 (1990) 649–655.

[15] R.A. Adomaitis, A ballistic transport and surface reaction model for simulating atomic layer deposition processes in high-aspect-ratio nanopores, Chem. Vapor Depos. 17 (2011) 353–365.

[16] R.G. Gordon, D. Hausmann, E. Kim, J. Shepard, A kinetic model for step coverage by atomic layer deposition in narrow holes or trenches, Chem. Vapor Depos. 9 (2003) 73–78.

[17] J. Dendooven, D. Deduytsche, J. Musschoot, R. Vanmeirhaeghe, C. Detavernier, Modeling the conformality of atomic layer deposition: the effect of sticking probability, J. Electrochem. Soc. 156 (2009) P63–P67.

[18] J. Elam, D. Routkevitch, P. Mardilovich, S. George, Conformal coating on ultrahigh-aspect-ratio nanopores of anodic alumina by atomic layer deposition, Chem. Mater. 15 (2003) 3507–3517.

[19] A. Yanguas-Gil, J.W. Elam, Self-limited reaction-diffusion in nanostructured substrates: surface coverage dynamics and analytic approximations to ald saturation times, Chem. Vapor Depos. 18 (2012) 46–52.

[20] T. Keuter, N.H. Menzler, G. Mauer, F. Vondahlen, R. Vaџen, H.P. Buchkremer, Modeling precursor diffusion and reaction of atomic layer deposition in porous structures, J. Vac. Sci. Technol. A 33 (2015) 01A104.

[21] C. Bae, H. Kim, E. Kim, H.G. Park, H. Shin, Atomic-layer deposition into 2-versus 3-dimensionally ordered nanoporous media: pore size or connectivity? Chem. Mater. 30 (2018) 4748–4754.

[22] A. Yanguas-Gil, Growth and Transport in Nanostructured Materials: Reactive Transport in PVD, CVD, and ALD, Springer, 2016.

[23] C.P. Andersen, H. Hu, G. Qiu, V. Kalra, Y. Sun, Pore-scale transport resolved model incorporating cathode microstructure and peroxide growth in lithium-air batteries, J. Electrochem. Soc. 162 (2015) A1135–A1145.

[24] F. Brunner, F.A. Radu, M. Bause, P. Knabner, Optimal order convergence of a modified BDM1 mixed finite element scheme for reactive transport in porous media, Adv. Water. Resour. 35 (2012) 163–171.

[25] S. Chen, G.D. Doolen, Lattice Boltzmann method for fluid flows, Annu. Rev. Fluid Mech. 30 (1998) 329–364.

[26] A. Xu, W. Shyy, T. Zhao, Lattice Boltzmann modeling of transport phenomena in fuel cells and flow batteries, Acta Mech. Sinica 33 (2017) 555–574.

[27] W.Z. Fang, Y.Q. Tang, L. Chen, Q.J. Kang, W.Q. Tao, Influences of the perforation on effective transport properties of gas diffusion layers, Int. J. Heat Mass Tran. 126 (2018) 243–255.

[28] A. Xu, L. Shi, T. Zhao, Accelerated lattice Boltzmann simulation using GPU and OpenACC with data management, Int. J. Heat Mass Tran. 109 (2017) 577–588.

[29] W.Z. Fang, J.J. Gou, L. Chen, W.Q. Tao, A multi-block lattice Boltzmann method for

the thermal contact resistance at the interface of two solids, Appl. Therm. Eng. 138 (2018) 122–132.

[30] Q. Kang, D. Zhang, S. Chen, X. He, Lattice Boltzmann simulation of chemical dissolution in porous media, Phys. Rev. E 65 (2002) 036318.

[31] Q. Kang, P.C. Lichtner, H.S. Viswanathan, A.I. Abdel-Fattah, Pore scale modeling of reactive transport involved in geologic CO_2 sequestration, Transport Porous Med. 82 (2010) 197–213.

[32] A. Parmigiani, C. Huber, O. Bachmann, B. Chopard, Pore-scale mass and reactant transport in multiphase porous media flows, J. Fluid Mech. 686 (2011) 40–76.

[33] L. Chen, R. Zhang, T. Min, Q. Kang, W. Tao, Pore-scale study of effects of macroscopic pores and their distributions on reactive transport in hierarchical porous media, Chem. Eng. J. 349 (2018) 428–437.

[34] F. Gray, J. Cen, E. Boek, Simulation of dissolution in porous media in three dimensions with lattice Boltzmann, finite-volume, and surface-rescaling methods, Phys. Rev. E 94 (2016) 043320.

[35] Z. Deng, W. He, C. Duan, B. Shan, R. Chen, Atomic layer deposition process optimization by computational fluid dynamics, Vacuum 123 (2016) 103–110.

[36] K. Wu, X. Li, C. Wang, W. Yu, Z. Chen, Model for surface diffusion of adsorbed gas in nanopores of shale gas reservoirs, Ind. Eng. Chem. Res. 54 (2015) 3225–3236.

[37] K.J. Lange, P.C. Sui, N. Djilali, Pore scale simulation of transport and electrochemical reactions in reconstructed PEMFC catalyst layers, J. Electrochem. Soc. 157 (2010) B1434–B1442.

[38] L. Chen, Q. Kang, R. Pawar, Y.L. He, W.Q. Tao, Pore-scale prediction of transport

properties in reconstructed nanostructures of organic matter in shales, Fuel 158 (2015) 650–658.

[39] L. Chen, L. Zhang, Q. Kang, H.S. Viswanathan, J. Yao, W. Tao, Nanoscale simulation of shale transport properties using the lattice Boltzmann method: permeability and diffusivity, Sci. Rep. 5 (2015) 8089.

[40] C.D. Shackelford, S.M. Moore, Fickian diffusion of radionuclides for engineered containment barriers: diffusion coefficients, porosities, and complicating issues, Eng. Geol. 152 (2013) 133–147.

[41] V.R. Cremers, R.L. Puurunen, J. Dendooven, Conformality in atomic layer deposition: current status overview of analysis and modelling, Appl. Phys. Rev. 6 (2019) 021302.

[42] M.C. Schwille, T. Schssler, J. Barth, M. Knaut, F. Schn, A. Hchst, M. Oettel, J.W. Bartha, Experimental and simulation approach for process optimization of atomic layer deposited thin films in high aspect ratio 3D structures, J. Vac. Sci. Technol. A 35 (2017) 01B118.

[43] J. Musschoot, J. Dendooven, D. Deduytsche, J. Haemers, G. Buyle, C. Detavernier, Conformality of thermal and plasma enhanced atomic layer deposition on a nonwoven fibrous substrate, Surf. Coat. Tech. 206 (2012) 4511–4517.

[44] L. Chen, G. Wu, E.F. Holby, P. Zelenay, W.Q. Tao, Q. Kang, Lattice Boltzmann pore-scale investigation of coupled physical-electrochemical processes in C/Pt and non-precious metal cathode catalyst layers in proton exchange membrane fuel cells, Electrochim. Acta 158 (2015) 175–186.